High-Definition Polymeric Membranes: Construction of 3D Lithographed Channel Arrays through Control of Natural Building Blocks Dynamics

Valentina Speranza,[†] Francesco Trotta,[‡] Enrico Drioli,[§,⊥] and Annarosa Gugliuzza*[,⊥]

Research Institute on Membrane Technology, National Research Council (ITM-CNR), I-87030 Rende (CS), Italy, Department of Pharmaceutical Science, University of Calabria, I-87030 Rende, Italy, Department of Chemistry, IFM, University of Turin, I-10125 Turin, Italy, and Department of Chemical Engineering and Materials, University of Calabria, I-87030 Rende, Italy

ABSTRACT The fabrication of well-defined interfaces is in high demand in many fields of biotechnologies. Here, high-definition membrane-like arrays are developed through the self-assembly of water droplets, which work as natural building blocks for the construction of ordered channels. Solution viscosity together with the dynamics of the water droplets can decide the final formation of three-dimensional well-ordered patterns resembling anodic structures, especially because solvents denser than water are used. Particularly, the polymer solution viscosity is demonstrated to be a powerful tool for control of the mobility of submerged droplets during the microfabrication process. The polymeric patterns are structured at very high levels of organization and exhibit well-established transport−surface property relationships, considered basics for any types of advanced biotechnologies.

KEYWORDS: structured material • polymeric architecture • ordered membrane • scaffold • interface • self-assembly • template

INTRODUCTION

Structured membranes at very high levels of order on lengths of micro- and nanoscale will be ambitious and attractive challenges of the coming years in many fields of material science, including membrane contactors (1, 2), sensors (3), and tissue engineering (4). The fabrication of high-definition architectures with desired properties through simple, solvent-reduced, and reproducible techniques is just in high demand. Time-consuming, pollutant, and too expensive standard practices are giving way to ecosustainable and flexible technologies, enabling the fabrication of breakthrough membranes (5–7), scaffolds (8, 9), platforms (10, 11), and photonics (12, 13) in shorter time and at more competitive costs. The choice for well-defined membrane-like arrays can be successful because ordered and controlled morphology takes advantage of promoting extensive processes in all regions of the interface, reproducibility of the events at long range, and then high sensitivity,

selectivity, and fast response/recovery times. Despite the fact that several advanced manufacturing processes have been proposed (14–16), nanosized templates and procedures with reduced numbers of steps are still ambitious challenges. In this work, water droplets are used as natural and well-sized building blocks for the fabrication, in only one step, of self-standing ordered polymeric membranes, exploiting strategically the intrinsic viscosity of the casting solutions. Here, three-dimensionally (3D) interconnected lithographed pores are designed in a few minutes through a time-saving, solvent-reduced, and economically competitive approach inspired by natural events like fog and water condensation from humid air, which yield well-defined and shaped water droplets working as real pore builders. These natural events can be reproduced in the laboratory by the cooling of casting solutions through solvent evaporation in a humid atmosphere. After condensation, submerging water droplets grow and self-assemble in ordered arrays, yielding a highly defined hexagonally packed geometry as a result of their imprinting action, different from what was observed for conventional phase separation techniques (17, 18). The droplet coalescence is outstandingly prevented by both the formation of a polymeric envelope around the droplets (19) and the effects of thermocapillary convection on gradients of temperature (20), which stabilize uniform water microspheres, making them solidlike particles. The water droplets, here referred to as "imprinting spheres", are left to organize directly into the liquid films through a balanced mechanism of solvent evaporation and water condensation from a humid atmosphere, which provides the real driving force for

* Corresponding author. E-mail: a.gugliuzza@itm.cnr.it or annarosa.gugliuzza@cnr.it. Phone: +39 0984 492026. Fax: +39 0984 402103.
Received for review October 15, 2009 and accepted December 21, 2009

⊥ Research Institute on Membrane Technology, National Research Council (ITM-CNR), Via P. Bucci 17/C, I-87030 Rende (CS), Italy.
† Department of Pharmaceutical Science, University of Calabria, Polifunzionale Building, I-87030 Rende, Italy.
‡ Department of Chemistry, IFM, University of Turin, Via Giuria 7, I-10125 Turin, Italy.
§ Department of Chemical Engineering and Materials, University of Calabria, Via Pietro Bucci 45A, I-87030 Rende, Italy.
DOI: 10.1021/am900701r

Scheme 1. Simplified Mechanism for the Formation of Template Figures
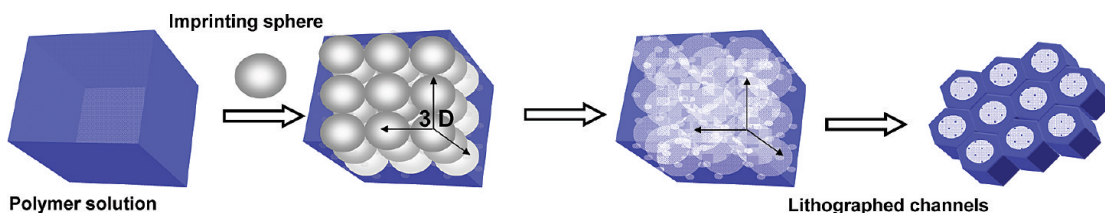
this lithographic process. Some authors (20, 21) intuited the capability of water to organize in mobile islands and template star-shaped and diblock copolymers, suggesting the air velocity across the polymer surface as the controlling factor for modulation of the pore size and use of a solvent lighter than water for the fabrication of 3D air-bubble arrays. In this work, we provide new breakthroughs about the crucial role of the polymer solution viscosity and droplet dynamics in the construction of 3D well-controlled architectures on the micro- and nanoscale, demonstrating how it is possible to form well-ordered pore networks at long range and through 3D space by using solvents denser than water. Specifically, the function of the polymer solution viscosity is examined in relation to the dynamics of the natural building blocks, demonstrating also how the achievement of high-definition architectures is relevant for control of the final structure–function relationships, including transmembrane diffusion and surface wettability. The experimental findings discussed here suggest these 3D lithographed channel arrays as promising high-performance interfaces for various advanced biotechnological applications.

MATERIALS AND METHODS

A nitrated poly(ether ether ketone) (PEEK-WC-NO$_2$) with different substitution degrees (SDs; 0.10, 0.16, 0.33, and 0.34) was synthesized by the addition of a sulfonitric mixture (0.92 mL of HNO$_3$ and 2.16 mL of H$_2$SO$_4$) to the powder of the precursor, a modified poly(ether ether ketone) with a CARDO group (PEEK-WC), and heating at 85 °C for 2 h. The purified nitrated polymer was then dissolved in three different chlorinated solvents [chloroform (CL), 1,2-dichloroethane (DCE), and dichloromethane (DCM)] at 1.0 wt %. The solutions were stirred at room temperature until homogeneous and clear dopes were achieved. The casting solutions were placed in clean and dried stainless steel supports and located inside a box equipped with sensors of temperature and relative humidity equilibrated at 70 % and 25 °C (Delta E Srl Co.). Depending on the viscosity, the casting solution became turbid in the first 30–50 s of exposure to humid air, while complete formation of the solid film occurred after 180–360 s as a function of the casting solution volume (0.5–1.0 mL). When formed, the membrane was detached from the support and further dried at room temperature. The viscosity of the various polymer dopes was measured at 200 rpm at 25 °C by using a programmable rheometer (Brookfield DV III ULTRA). Membrane morphology and topography were investigated by scanning electron microscopy (SEM; Quanta FENG 200, FEI Company), confocal laser scanning microscopy (Olympus Italia), and atomic force microscopy (AFM; Nanoscope III Digital Instruments, VEECO Metrology Group). The average membrane surface roughness (R_a, nm) was estimated by an AFM tapping mode instrument, which was operated in air by scanning a tip attached to the end of an oscillating cantilever across $10 \times 10 \ \mu m^2$ and $30 \times 30 \ \mu m^2$ of the sample surface at a rate of 1.0 Hz. The pore size, pore distribution, and surface porosity were estimated from SEM images by using *Image J*, version 1.37, software. The pore size had a log-normal distribution for all membranes and was expressed by the probability density function according to the procedure described in ref 22. The cumulative distribution function was obtained for each single membrane by plotting the median rank on the ordinate versus the ascending pore size on the abscissa and was a straight line on log-normal probability paper with correlation coefficients r^2 from 0.91 to 0.98. The surface porosity was calculated as the ratio between the area of the pores to the total membrane surface area (22). The overall porosity was measured by weighing the amount of a perfluorinated hydrocarbon at low surface free tension (Fluorinert FC40, 3 M Novec) adsorbed inside of the membrane pores. The interconnectivity of the air cavities was also evaluated through water vapor transmission rate measurements according to the gravimetric method. The membrane-sealing flasks filled with ultrapure water were equilibrated for 1 h at 25 °C and, then, located in a box containing a desiccant. The loss of water vapor was estimated after 24 h, and the transmission rate was expressed as a ratio of the weight variation of the water and the membrane area per day [g/(m^2 · day)]. In order to detect how the high-definition textures affect the final membrane surface properties, the spreading behavior of polar and nonpolar solvents was also evaluated through kinetic contact-angle experiments by a sessile drop method. The apparent water and isooctane contact-angle values were measured with standard deviations of less than ±3° and ±4°, respectively. The liquid probe droplets were dispensed and deposited on the membrane surface by using a microsyringe with an automatic dispenser, and the images were captured with time by a digital camera (CAM 200-KSV Instrument Ltd., Helsinki, Finland).

RESULTS AND DISCUSSION

Viscosity Polymer Solution, High-Definition Architectures, and Structure–Function Relationships. The manufacturing approach inspired by the natural condensation of humid air on cold surfaces is one of the most fascinating breakthroughs in the fabrication of membranes with well-defined and desired structural features (Scheme 1). Despite the fact that the technique seems to be easy to handle, the mechanisms leading to the formation of high-definition polymeric architectures appear to be rather complicated and in need of further study. Various controlling factors and mechanisms have been taken into account to explain the behavior of the droplet lattices during the tailoring procedure (20, 21, 23), but an unambiguous interpretation of the events is still expected. Although the occurrence of mixed mechanisms cannot be excluded, it is very important to consider the role of specific controlling factors for interpreting correctly the experimental findings. In this study, we offer new insights into the identification of a crucial factor, such as the polymer solution viscosity, that can also decide the architecture and texture of polymer

Scheme 2. Synthesis of PEEK-WC-NO₂ via Nitration of the Parent PEEK-WC

PEEK-WC $\xrightarrow[\Delta]{HNO_3/H_2SO_4}$ PEEK-WC-NO₂
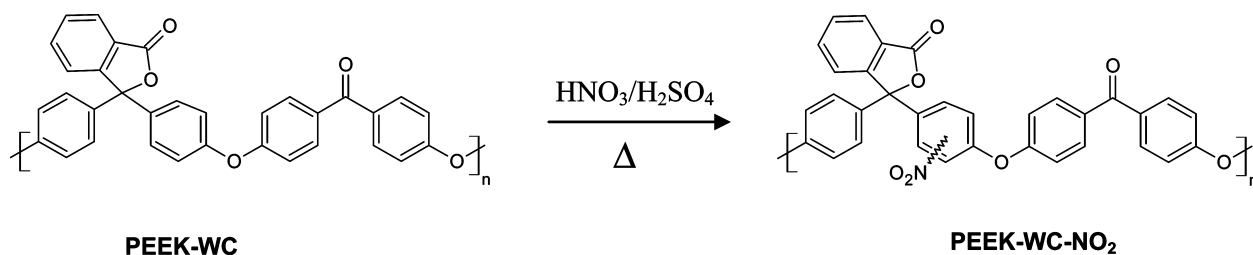
patterns when unusual experimental boundary conditions are selected. Here, this parameter is meant to be a powerful and feasible tool, enabling one to tailor polymer architectures through 3D space and achieve very high levels of organization, structure, and dynamics when solvents denser than water are used. In particular, self-standing membranes have been patterned in hexagonally packed geometries from a modified PEEK-WC-NO₂ (18), synthesized via nitration of PEEK-WC (Scheme 2) (24). The nitration of the polymer chain caused the polymer viscosity to decrease, affecting the dynamics of the water droplets. The resulting effects have been examined in relation to the construction of 3D high-definition architectures, considered to be responsible for well-established membrane structure−function relationships.

From Two-Dimensional (2D) to 3D Architectures through Control of Dynamics. The propagation of imprinting spheres through columns of solvents denser than water is traditionally unexpected. Usually, water droplets float on a denser liquid surface, forming monolayered arrays with traditional 2D air-bubble structures. Here, the formation of multilayers from chlorinated solutions through favored dynamics of the imprinting spheres is reported (Figure 1). Although surprising and promptly unexplainable, the event could be ascribed to the kinetics of the water

droplets when going from the vapor to liquid phase as well as established the viscosity parameters of the medium. In nature, water droplets are usually formed when hot humid air meets stratified cold air, resulting in precipitation. This event may occur when thermally controlled humid air is fluxed on cooled casting solutions, establishing a difference of temperature between the humid air and the surface and, then, causing precipitation of the uniformly cooled water droplets, which gather speed. Speeding and convection forces drag the water droplets into the casting solution, overcoming the initial resistance of denser liquid films and crystallizing in hexagonally ordered lattices via self-assembly. Formation and stabilization of each single layer occur as submerged droplets cover the whole area exposed to humidity and the local differences of temperature are dissipated. Shimomura et al. (23) suggested that thermocapillary and Marangoni forces directly cause the water droplets to submerge into the organic solution, preventing their levitation and self-assembly on the liquid surface. Then, these convective forces exerted on the submerged droplets facilitate the formation of lattices with a hexagonally packed geometry. Other authors (20) proposed a contradictory mechanistic pathway, suggesting the organization of the droplets on the entire surface and, then, their submersion into the liquid film. The experimental findings discussed here strengthen Shimomura et al.'s hypothesis, suggesting the coupling of convection forces with speedy droplets as a critical key element for interpretation of the mechanisms controlling this type of lithographic process. Indeed, the role of dynamics of the droplets is also suggested by stretched profiles of the pores, forming the latest layer of the bubble array (Figure 2a). When the event is almost about to the end, a large part of the solvent is just evaporated and a significant increase in the polymer viscosity is produced, causing major resistance to the penetration of the droplets and leaving, then, lengthened shapes of the air bubbles. On the other hand, the viscosity of the path is also suggested as another decisive element for penetration of the droplets through the column of the liquid films. The propagation of speedy cooled droplets is favored through less viscous liquids that offer lower resistance to their motion, whereas it is dramatically prevented through much more viscous paths, yielding a reduced number of pore layers and progressive densification of the bottom strata of the film (Figure 2b). Thus, a suitable balance between the dynamics of the droplets, convection forces, and viscosity of the solution can successfully direct
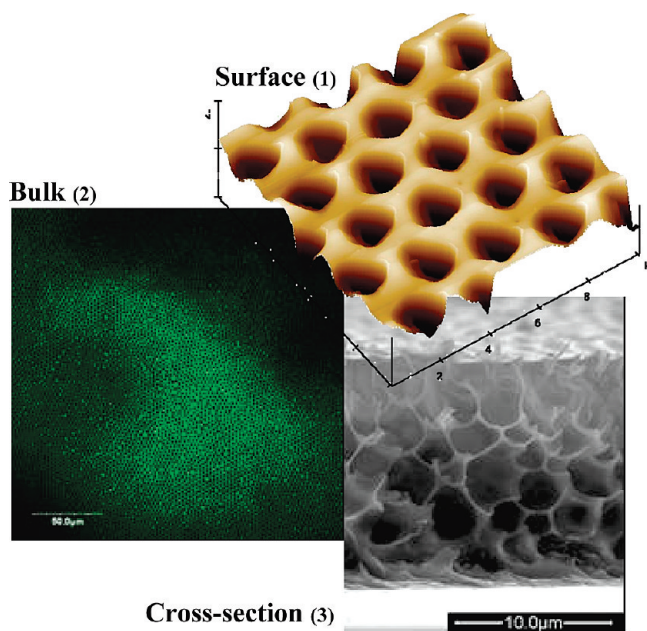

FIGURE 1. 3D well-ordered honeycomb structures patterned from PEEK-WC-NO₂: (1) top view collected by AFM; (2) layer collected in the bulk of the film by confocal microscopy; (3) SEM micrograph elucidating the cross section.
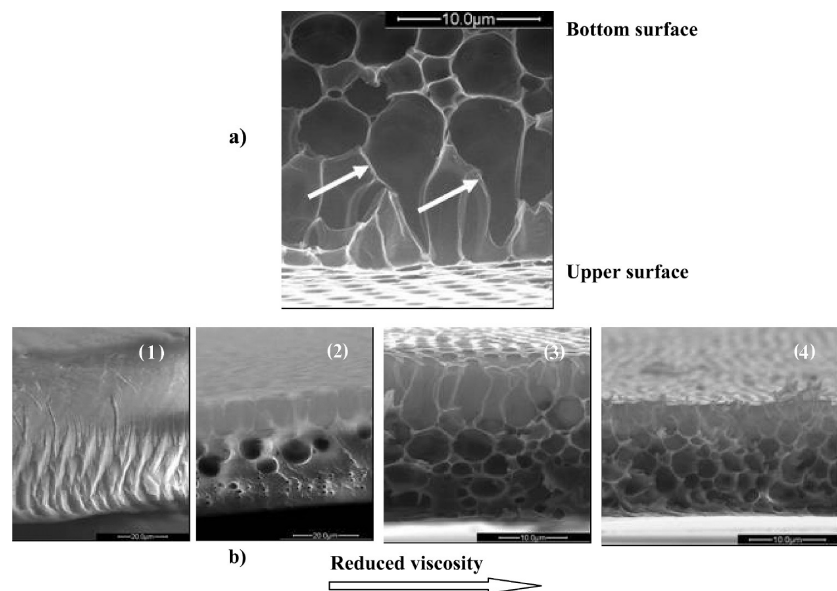
FIGURE 2. Water droplet propagation through the liquid film at different viscosities. (a) SEM micrograph illustrating the stretched pore shape in the upper layer of the polymer array. (b) SEM micrographs of the cross sections related to polymer arrays prepared from solutions having decreasing viscosities: (1) $\eta = 4.17$ cP; (2) $\eta = 1.50$ cP; (3) $\eta = 1.30$ cP; (4) $\eta = 1.17$ cP.

the construction of 3D well-ordered channel arrays also when solvents denser than water are used.

Bulk Structure and Molecule Diffusion. Another important concern is about the interconnection among air bubbles imprinted by the droplets. Flexibility and suitability of these microfabricated membranes are necessarily linked to this specific structural feature. The formation of open big bubbles represents, in fact, an important structural target for the diffusion of species through self-standing membrane-like arrays to be used in advanced separation and biomimetic processes. In order to establish the degree of interconnectivity among the pores, experiments of water vapor permeation and measurements of the overall porosity have been done, providing useful indications about structure−transport relationships. Increasing water permeation is usually measured as the membrane void volume fraction rises (Figure 3a). Instead, a dramatic abatement of the transmembrane flux can be observed as the propagation of the pore lattice is prevented through very high viscous media (Figure 2b). A uniform and complete distribution of ordered big pores is not, however, enough to justify the reduced resistance to the transport. High interconnectivity of the pores is, in turn, requested to promote large volumetric mass-transfer rates through the membranes. Thus, the membranes were dipped in a liquid at low surface free tension and the amount of liquid adsorbed was weighted, yielding useful indications about the interconnectivity degree. The amount of liquid was, then, related to the overall void volume fraction, resulting in values up to 85 % as the propagation of the pore lattice was completed. SEM reveals effectively the presence of connecting nanopores into the bulk of the membranes (Figure 3b). An interesting question is about the cause of the formation of these smaller pores. During their growth, the water droplets displace efficiently a polymer solution as large as the extension of their volume is, forming the biggest pores. When submerged, the droplets
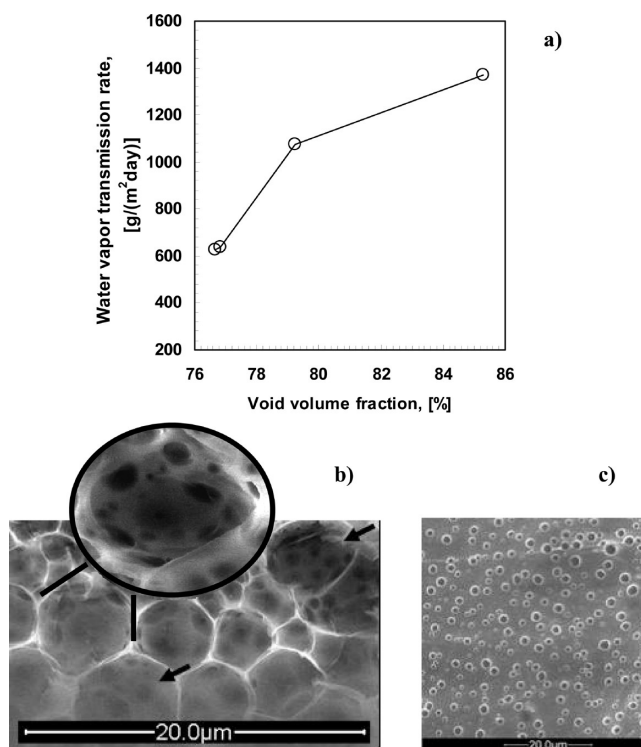

FIGURE 3. Structure−transport relationships: (a) Estimation of the water transmission rate through high-definition patterns exhibiting increasing void volume fractions. (b) SEM micrographs showing the uniform distribution of nanopores through the walls of the biggest air bubbles. (c) SEM micrograph showing uniform and well-shaped nanopores on the bottom surface of the polymer arrays.

cause also a precipitated-like state for the polymer around themselves. Pitois and Francois (19) argued that the polymer envelope inhibits mutual interactions and prevents complete coalescence of the droplets and the consistency of this stratum is all the more significant as the polymer concentration increases in solution. In our case, the formation of numerous connecting nanosized pores through the biggest

bubbles may also be interpreted on the basis of these experimental findings. It is plausible, in fact, to think that a near-precipitated polymer layer at the water–solution interface opens up where the film is too lean. A reduction of 1 order of magnitude in the pore size moving from the upper to lower surfaces (Figure 3c) can also be a concern as a consequence of the weak encapsulating action of the polymer in proximity to neighboring surfaces, resulting in films with double well-sized porous surfaces. These particular structure–transport relationships make these interfaces interesting and attractive for various applications, including contactors and scaffolds for tissue engineering. In the first case, the very high level of organization and structure of the pores and their low resistance to the mass transfer represent two challenging goals for membrane contactor devices, where the membrane works as a physical interface between two media, preventing them from mixing and promoting mass transfer by diffusion. In this case, a uniform pore distribution and a high volume void fraction enable full satisfaction of two important basics of the membrane contactor technology: a higher interfacial area per unit volume and a higher volumetric mass-transfer rate. Concerning the potential use of these polymeric patterns in tissue engineering, the combination of two different pore sizes could also provide suitable mimetic structural microenvironments for promoting the adherence and growth of cells inside the biggest pores and the simultaneous diffusion of nutrients and metabolites through the smallest channels. On the other hand, controlled scaffold structures are also envisaged to provide local environments to adaptive biosystems, coming closer to living matter through aimed combinations of physical, chemical, and structural properties.

Texture of the Membrane Surface. *Chemical Substitution and Polymer Viscosity.* Self-standing membranes have been patterned in hexagonally packed geometries from PEEK-WC-NO$_2$ at different SDs in order to evaluate the influence of the nitro group on any of the intrinsic properties of the polymer solutions, including the viscosity. An increase in the degree of chemical substitution of the polymer chains effectively causes a reduction in the polymer solution viscosity because the steric hindrance of the pending nitro moiety limits the degree of entanglements of the polymer chains. Here, the viscosity is also speculated to be a driving-force parameter for the construction of well-defined surface textures (Figure 1). Depending on the polymer viscosity, the final pore size and ordered geometry can successfully be directed on the polymer surface through controlled mobility of the submerged droplets. The membrane topography is a result of the velocity of the imprinting spheres to self-assemble during the latest stage of the lithographic process (Figure 4). In order to establish the role of the polymer viscosity in the rapidity of rearrangement and crystallization of the droplets, equal amounts of PEEK-WC and PEEK-WC-NO$_2$ at increasing SDs were dissolved in the same chlorinated solvent, yielding polymer dopes at decreasing viscosities (Figure 5a). It has been observed that condensed droplets are free to move more quickly through

media at lower viscosity, forming well-sized and highly ordered lattices in a shorter time (Figure 4a_3). As was aforementioned, the layers, including the last one, form and stabilize as submerged droplets cover the whole area exposed to humidity and local differences of the temperature are dissipated. Therefore, the formation of smaller-sized and monodisperse pores is the result of a much quicker coverage by the imprinting spheres through less viscous liquid films (Figure 4a_3). Differently, coverage of the whole area and ordered reorganization are slowed down at higher viscosity. In this case, the growth rate of the imprinting spheres is extended and the droplet mobility is affected, and as a result, slightly larger pores and no perfectly ordered geometry are sometimes obtained (Figure 4a_1,2).

Solvent Viscosity. More significant differences in the pore size can occur as PEEK-WC-NO$_2$ at the same SD is dissolved in chlorinated solvents with different viscosities. Experimental findings highlight once more the crucial role of the mobility of the droplets in patterning polymer solutions (Figure 4b_4–6). As was discussed, a higher polymer solution viscosity slows down somewhat the coverage of the whole area of the casting solution exposed to humid air, extending the growth stage of the droplets. This yields the larger top hemisphere of the imprinting spheres in contact with air during the formation of the latest layer, resulting in an increased sphere diameter up to 5.0 μm as CL, for instance, is used (Figure 4b_4). Differently, lower viscosity leads more quickly to the formation of channels with sizes of less than 1 order of magnitude (0.9 μm) as the solvent is changed from CL to DCM (Figures 4b_5–6 and 5b). Some authors (25) speculated that the size of the droplets is decided by the evaporation velocity of the solvent and, therefore, by the difference of the temperature between the liquid surface and humid air. The higher the solvent boiling point, the lower the volatility. A decrease in the difference of the temperature delays, therefore, the coverage of the whole area of the casting solution. This causes an enrichment of the submerged droplet volume, waiting for the formation of one stable and defined layer. Undoubtedly, a slower droplet condensation and a more extended growth rate are expected when a solvent like CL with a higher boiling point ($T_{bp} = 61$ °C, $M_w = 119.38$ Da, and $d_{20 °C} = 1.47$ g cm^{-3}) is used, yielding enlarged pores (Figure 4b_4). Differently, solvents with higher volatility such as DCM ($T_{bp} = 40$ °C, $M_w = 84.93$ Da, and $d_{20 °C} = 1.33$ g cm^{-3}) yield quicker coverage and self-assembly of submerged droplets, leaving smaller air bubbles for the effect of an enhanced difference of the temperature (Figure 4b_6).

However, considering that films with a mean pore size of 1.3 μm have also been fabricated from PEEK-WC-NO$_2$ dissolved in DCE ($T_{bp} = 83$ °C, $M_w = 98.97$ Da, and $d_{20 °C} = 1.25$ g cm^{-3}), the volatility of the solvent seems to be not such a decisive parameter for the final pore size (Figure 4b_5). Rather, the different molecular weights of the solvents can significantly affect the velocity of the solvent evaporation for the effect of an increased solution viscosity, causing also
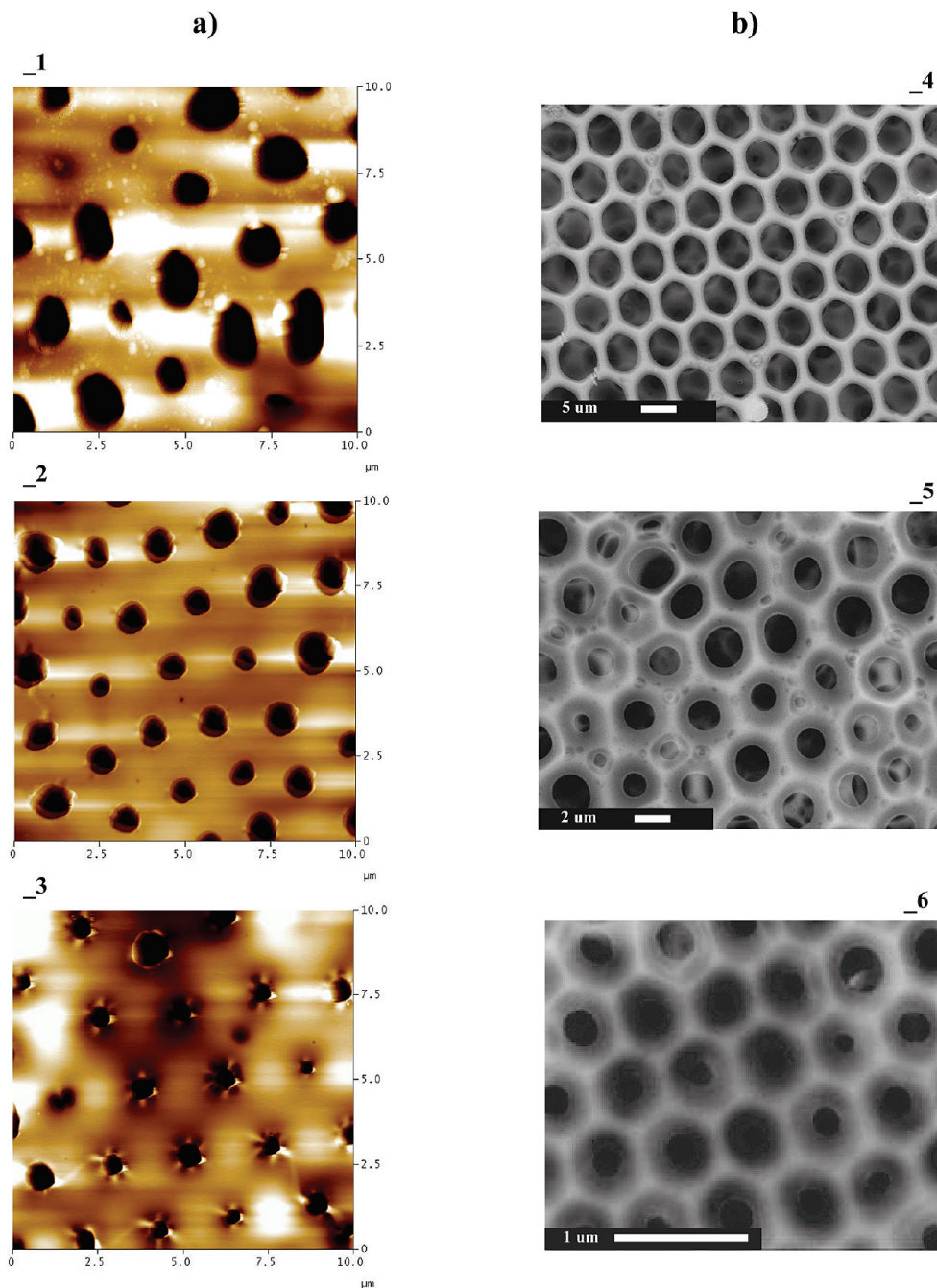
a)

b)

FIGURE 4. Effects of the polymer chemical SD and solvent on the final membrane texture. (a) AFM images elucidating changes in the order and pore size as the polymer viscosity decreases for the effect of increased nitration degree of the polymer: PEEK-WC-NO$_2$ (SD: 1, 0.10; 2, 0.16; 3, 0.33) dissolved in DCM at 1.0 wt %. (b) SEM micrographs of bubble arrays achieved from solutions of PEEK-WC-NO$_2$ with nitration of SD = 0.34 and prepared from (4) CL, (5) DCE, and (6) DCM solutions, respectively.

a diminution of the velocity of the imprinting spheres to cover the whole area and rearrange in semicrystalline lattices.

In summary, very high levels of organization of the pores are achieved as polymer solutions at lower viscosity are imprinted by natural building blocks. Specifically, high-definition textures are achieved for PEEK-WC-NO$_2$ at higher degrees of chemical substitution (i.e., SD = 0.33 and 0.34), whereas the pore size can be modulated through control of the solvent viscosity.

Lithographed Texture and Well-Defined Surface Properties. To establish the influence of the mor-

phology on any intrinsic features of the films, some structure–function relationships have also been speculated. High bulk porosity (Figure 2) as well as very high interfacial area (Figure 6a,b) are derived from high-definition air-bubble arrays. The second one depends significantly on the surface morphology and is particularly regarded as a key structural element to reproduce simultaneous events in all regions of the film and yield highly productive and sensitive processes. Well-defined surface textures can positively affect the final surface properties, resulting also in well-established mutual liquid–surface interactions. With this regard, particularly enhanced waterproofness has been estimated, for example,
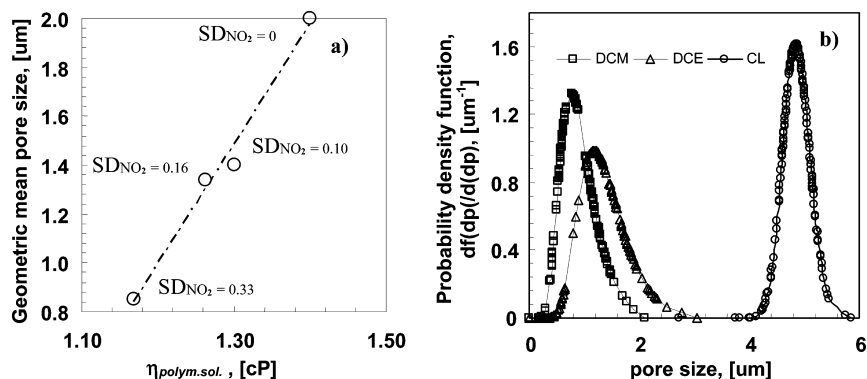
ACS APPLIED MATERIALS & INTERFACES Speranza et al.

FIGURE 5. Solution–structure relationships: (a) Changes in the geometric mean pore size versus increasing viscosity of the polymer solutions, where SD_{NO_2} is the substitution degree. (b) Changes in the pore size and distribution as a function of the solution viscosity caused by the solvent used.
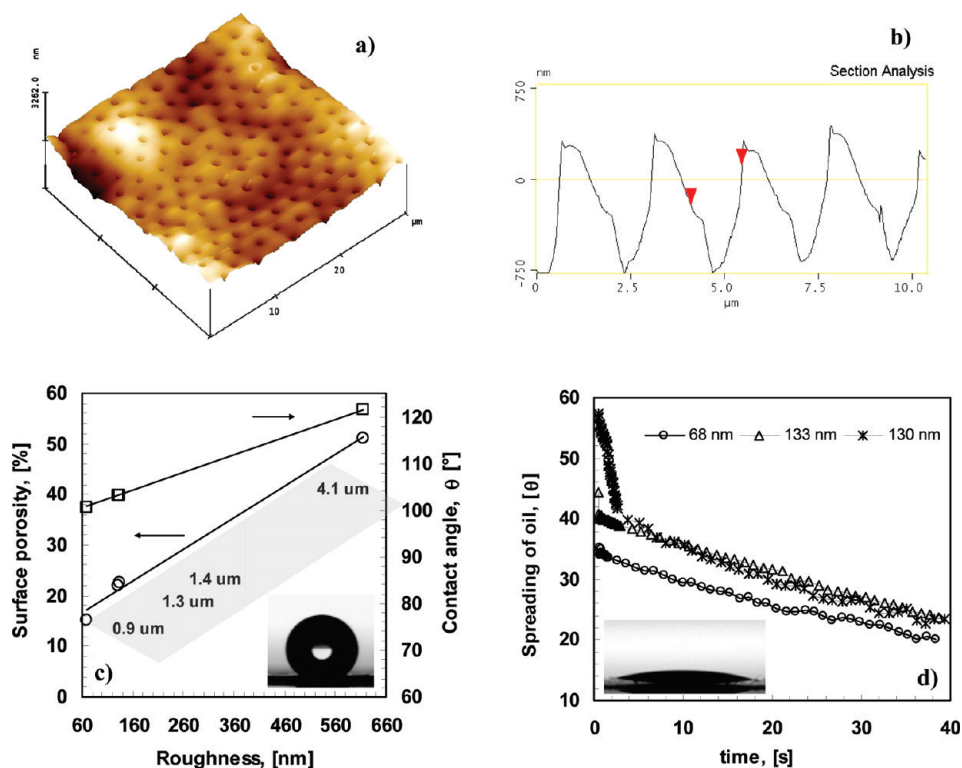

FIGURE 6. Topography–surface property relationships: (a) AFM images displaying a high level of organization of lithographed channels at long range: $30 \times 30 \ \mu m^2$ of the sample surface. (b) Section analysis of the honeycomb texture evaluated via AFM. (c) Relationship between the pore size, surface porosity, and roughness and dependence of the water contact angle on the surface roughness. (d) Quick spreading of isooctane on patterned surfaces as a function of the surface roughness.

for tailor-made PEEK-WC-NO_2 membranes as the surface roughness increased (Figure 6c).

It is well-known that the wettability of the solid surfaces with water is influenced by two main factors such as surface chemistry and surface topography. Considering that no chemical modifications occurred on the surface of these patterns and water contact-angle values of 80 °C are usually measured on PEEK-WC-NO_2 membranes prepared by traditional phase inversion (18), the improved water repellence can be ascribed to the singular surface texture and, distinctively, to the effects of the surface roughness to produce composite surfaces. Indeed, membrane surfaces become rougher as the pore size and surface porosity grow (Figure 6c), suggesting an inherent dependence on the pore diameter. Because the average roughness R_a is defined as the

average deviation of the peaks and valleys from the mean plane, the distribution and average distance between the edge and depth of the single pores affect significantly the surface roughness, as was predicted and measured from AFM images (Figures 4 and 6a,b). On the other hand, an increase in the pore size is also expected to lead to increased surface porosity, with the latter being defined as the ratio of the pore area to the total area of the membrane (Figure 6c).

However, the question is, why does the apparent contact angle increase with surface roughness? It was found that a material becomes water-repellent if air is enclosed between the surface structures and an applied water droplet (26, 27). Indeed, the ordered sequence of well-shaped pores causes a "zig-zag" profile that produces a hierarchical roughness enough to capture air inside the hexagonally packed pores

(Figure 6b). Thus, a composite interface that reduces the adhesion line between the water droplets and the substrate is formed, resulting in less resistance to the motion of the droplets than that of a full contact area. In this way, the surface void fraction of the area (i.e., pores) under the water drop increases, and as a result, the drops sit on more air than solid and the film becomes more hydrophobic (Figure 6c).

A similar dependence on the surface roughness can also be observed for hydrophobic liquid probes such as isooctane (Figure 6d), although the lowest surface free tension promotes quick spreading, providing a useful indication about its facilitated penetration inside the membrane pores. These peculiar structure−surface relationships make these polymeric patterns potential breakthrough membranes for advanced oil/water membrane emulsifiers (28, 29), considering that the high level of organization of the well-defined pore geometry and the absence of coalescence phenomena can be decisive for the size, shape, and uniformity of droplets dispersed in a continuous phase, whereas controlled wettability can facilitate the dispersion of droplets of a liquid in a continuous phase through transmembrane permeation.

CONCLUSIONS

This study identifies the mobility of the water droplets as a key controlling factor that decides the final pore size, order degree, and complete lattice propagation of high-definition membranes through space. The manufacturing approach is inspired by the natural condensation and self-assembly of water droplets, working as pore builders. The construction of 3D channel arrays from solutions denser than water can be ascribed to a suitable combination of cooled droplets that gather speed during their precipitation from humid air and control of the polymer solution viscosity. In the same way, the membrane topography is the result of different mobilities of submerged water droplets through viscous media.

The singular architecture of these interfaces is regarded as a decisive issue for achieving well-established structure−function relationships in terms of transport and surface properties, resulting in attractive lithographed membranes to be operated in various technologically sophisticated applications.

REFERENCES AND NOTES

(1) Gugliuzza, A.; Aceto, M. C.; Macedonio, F.; Drioli, E. *J. Phys. Chem. B* **2008**, *112* (34), 10483−10496.
(2) Lambrich, U.; Schubert, H. *J. Membr. Sci.* **2005**, *257*, 76−84.
(3) Batley, H.; Braha, O.; Gu, L. Q. *Adv. Mater.* **2000**, *12*, 139−142.
(4) Landis, F. A.; Stephens, J. S.; Cooper, J. A.; Cicerone, M. T.; Lin-Gibson, S. *Biomacromolecules* **2006**, *7* (6), 1751−1757.
(5) Cardea, S.; Gugliuzza, A.; Sessa, M.; Aceto, M. C.; Drioli, E.; Reverchon, E. *ACS Appl. Mater. Interfaces* **2009**, *1* (1), 171−180.
(6) Wu, S.; Park, S. R.; Ling, X. S. *Nano Lett.* **2006**, *6* (11), 2571−2576.
(7) Bohaty, A. K.; Zharov, I. *Langmuir* **2006**, *22* (13), 5533−5536.
(8) Liu, Y.W. S.; Lee, J. W.; Kotov, N. A. *Chem. Mater.* **2005**, *17* (20), 4918−4924.
(9) Velev, O. D.; Lenhoff, A. M.; Kaler, E. W. *Science* **2000**, *287*, 2240−2243.
(10) Park, S.; Lee, K. B.; Choi, I. S.; Langer, R.; Jon, S. *Langmuir* **2007**, *23* (22), 10902−10905.
(11) Holden, M. A.; Needham, D.; Bayley, H. *J. Am. Chem. Soc.* **2007**, *129* (27), 8650−8655.
(12) Imhof, A.; Pine, D. J. *Nature* **1997**, *389*, 948−951.
(13) Lotsch, B. V.; Ozin, G. A. *ACS Nano* **2008**, *2* (10), 2065−2074.
(14) Velev, O. D.; Jede, T. A.; Lobo, R. F.; Lenhoff, A. M. *Nature* **1997**, *389*, 447−448.
(15) Yi, G. R.; Moon, J. H.; Manoharan, V. N.; Pine, D. J.; Yang, S. M. *J. Am. Chem. Soc.* **2002**, *124*, 13354−13355.
(16) Imhof, A.; Pine, D. J. *Adv. Mater.* **1998**, *10*, 697−700.
(17) Wienk, I. M.; Boom, R. M.; Beerlage, M. A. M.; Bulte, A. M. W.; Smolders, C. A.; Strathmann, H. *J. Membr. Sci.* **1996**, *113* (2), 361−371.
(18) Trotta, F.; Drioli, E.; Gordano, A. *J. Appl. Polym. Sci.* **2001**, *80*, 1037−1045.
(19) Pitois, O.; Francois, B. *Eur. Phys. J. B* **1999**, *8*, 225−231.
(20) Srinivasarao, M.; Collings, D.; Philip, A.; Patel, S. *Science* **2001**, *292*, 79−83.
(21) Pitois, O.; Francois, B. *Colloid Polym. Sci.* **1999**, *277*, 574−578.
(22) Khayet, M.; Feng, C. Y.; Matsuura, T. *J. Membr. Sci.* **2003**, *213*, 159.
(23) Maruyama, N.; Koito, T.; Nishida, J.; Sawadaishi, T.; Cieren, X.; Kjiro, K.; Karthaus, O.; Shimomura, M. *Thin Solid Films* **1998**, *327*, 854−856.
(24) Zhang, H. C.; Chen, T. L.; Yuan, Y. G. Chinese Patent CN 85,108,751, 1987.
(25) Tian, Y.; Jiao, Q.; Ding, H.; Shi, Y.; Liu, B. *Polymer* **2006**, *47*, 3866−3873.
(26) Holloway, P. J. *Pest. Sci.* **1970**, *1*, 156−163.
(27) Abdelsalam, M. E.; Bartlett, P. N.; Kelf, T.; Baumberg, J. *Langmuir* **2005**, *21*, 1753−1757.
(28) Yanagishita, T.; Tomabechi, Y.; Nishio, K.; Masuda, H. *Langmuir* **2004**, *20* (3), 554−555.
(29) Giorno, L.; Piacentini, E.; Mazzei, R.; Drioli, E. *J. Membr. Sci.* **2008**, *317*, 19−25.

AM900701R